A Power Class Interoperable Reconfigurable Topology for Wireless Charging of EVs

Chao Liu, Mingzhu Zhou, Yizhan Zhuang, *Member, IEEE*, Xiangpeng Cheng, *Member, IEEE*, Xingkui Mao, *Member, IEEE*, and Yiming Zhang, *Senior Member, IEEE*

***Abstract*—Electric vehicle (EV) wireless power transfer (WPT) system is an important technical path to deal with the global energy crisis and reduce greenhouse gas emissions. By combining the different power classes exhibited by EVs in various scenarios, a reconfigurable topology for the WPT system of EVs was proposed, which can realize the switching of three different power classes without designing additional parameters, and fixing inputs. The proposed adopts power-class interoperability among SAE WPT1 (<3.70 kW), WPT2 (2.96–7.70 kW), and WPT3 (6.16–11.10 kW) power classes, and uses common unipolar and bipolar coils as the magnetic coupling structure for implementation. The purpose is to meet the power class quotas required in different charging periods or different charging scenarios. A 1.6-kW downscaled experimental prototype was established. Under the premise of 100 V input voltage, the maximum system dc–dc efficiency of 90.31%, 92.23%, and 94.02% of the three modes is achieved, respectively. By building a full-power simulation model, regardless of which mode the proposed system operates in, it remains within the safe range of electromagnetic radiation. Finally, in the case of misalignment, the function of the system in anti-misalignment is verified.**

***Index Terms*—Electric vehicles (EVS), interoperability, power class, reconfigurable topology, wireless power transfer (WPT).**

I. Introduction

AS AN important technological path to cope with the global energy crisis and reduce greenhouse gas emissions [1], [2], [3], [4], [5], [6], wireless power transfer (WPT) system for electric vehicles (EVs) [7], [8], [9] is expected to show a significant growth in the penetration rate of its transportation system. The American Electric Power Research Institute predicts that the penetration rate will reach 35%, 51%, and 62% in 2020, 2030, and 2050, respectively [10]. However, the large-scale development of EVs poses a severe challenge to the existing power distribution system: the overlap between the centralized nighttime residential charging demand and the traditional household load peak may lead to stability problems such as voltage fluctuations and power flow exceeding limits of the distribution network [11], [12].

TABLE I
SAE Standard Airgap and Power Class Correspond to Dimensional Parameters

Power class \ Airgap	Z1 (100-150 mm)	Z2 (140-210 mm)	Z3 (170-250 mm)
WPT1 (<3.70kW)	260×260 mm Φ4.5 mm	318×318 mm Φ9.0 mm	420×420 mm Φ5.0 mm
WPT2 (2.96-7.70kW)	250×250 mm Φ7.0 mm	320×320 mm Φ8.0 mm	380×380 mm Φ10.0 mm
WPT3 (6.16-11.10kW)	270×270 mm Φ7.0 mm	320×320 mm Φ8.0 mm	380×380 mm Φ10.0 mm

As more and more EV WPT systems are proposed and gradually put into use, the ideal charging scenario also needs to be replaced by a practical variety of application scenarios [13], [14], [15], [16]. When the EV WPT system is used in the old power grid or battery protection, the power class transmitted by the system is reduced as much as possible, which can protect the battery and extend the battery life [17]. For home or commercial charging, the balance between economy and efficiency can be ensured under the premise of ensuring the rated charging power [18]. For emergency power-up or high-value service scenarios, a higher output power class is necessary [19]. Only considers the scenario where the input voltages are consistent, that is, the scenario for home and commercial use [20]. However, the multiple and complex power class scenarios mentioned above put tremendous pressure on EV WPT systems. To alleviate this pressure and enable the WPT system to be applicable in various power class scenarios, the power class adaptation can be achieved from the following perspectives.

A. Magnetic Coupling Structure

Considering the characteristics of the WPT system, the switching between high-power-class coils and low-power-class coils is the most direct way of power class adaptation. By using the method of selectively energizing coils, low-power single-coil transmission can be achieved on the basis of a 20-kW multi-coil system [21]. Although there is a high-power multi-coil magnetic element and a low-power single-coil that can achieve power class adaptation mainly through magnetic couplers, it has not been proven through experiments that their respective systems perform well under low-power and high-power operations. In the context of multi-coil switching, a 50-kW three-phase WPT system with multiple coils was proposed. This system operates

Received 31 May 2025; revised 18 July 2025, 21 August 2025, and 11 September 2025; accepted 1 October 2025. Date of publication 9 October 2025; date of current version 23 December 2025. This work was supported by the National Natural Science Foundation of China under Grant 52577187. Recommended for publication by Associate Editor M. Ponce-Silva. *(Corresponding authors: Xiangpeng Cheng; Yiming Zhang.)*

The authors are with the School of Electrical Engineering and Automation, Fuzhou University, Fuzhou 350108, China (e-mail: 220110002@fzu.edu.cn; 220110005@fzu.edu.cn; zyz_joe@fzu.edu.cn; cxp@fzu.edu.cn; mxk782@fzu.edu.cn; zym@fzu.edu.cn).

Color versions of one or more figures in this article are available at https://doi.org/10.1109/TPEL.2025.3619511.

Digital Object Identifier 10.1109/TPEL.2025.3619511

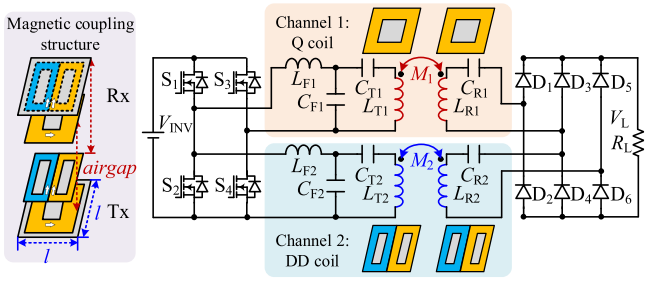

Fig. 1. Proposed power-class interoperable reconfigurable topology.

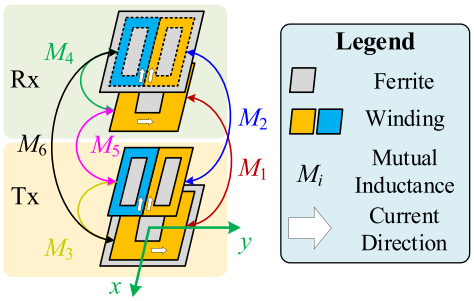

Fig. 2. Magnetic coupling structure in the proposed WPT system.

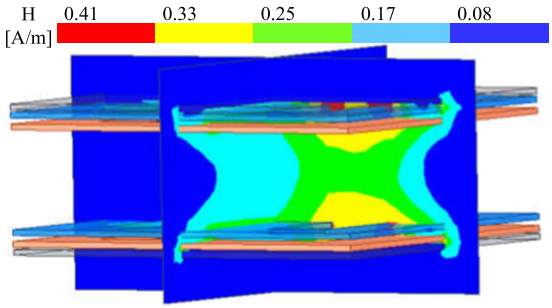

Fig. 3. Simulation model of the coupling structure.

at a reduced power class (5.0-kW), which is achieved by driving only one of the three coils on the transmitter (Tx) with a significantly reduced dc-bus voltage [22], [23]. In the context of power class interoperability, a balanced multicoil WPT system that can short-circuit or open-circuit one or more coils has advantages over an equivalent single-coil WPT system. This has established the advantage of the multi-transmission channel system in achieving interoperability of power classes.

B. Control Strategy

The power regulation methods within the WPT system are mainly manifested at the bilateral control level. In addition to using the method of adding additional switch hardware [24], the bilateral control also utilizes the active switch on the receiver (Rx) to regulate power. The bilateral control can adopt the form of a robust dc side regulator [25], using the active switch on the *Rx* to regulate power. It can also use a complex half/full-bridge active rectifier, which has Rx phase-shift angle control or Rx active bridge relative to Tx phase-shift control [26], [27], [28], [29]. However, the cost of bilateral control is higher than the single-side power regulation technology, but it reduces the component cost compared to adding additional switch hardware. At the same time, even if zero voltage switching (ZVS) is satisfied, not only will the efficiency presented by the system decrease, but the loss of the switching devices will be higher than in the case of single-side power regulation.

In the context presented above, WPT system with power-class interoperability performance needs to be proposed in [29] and

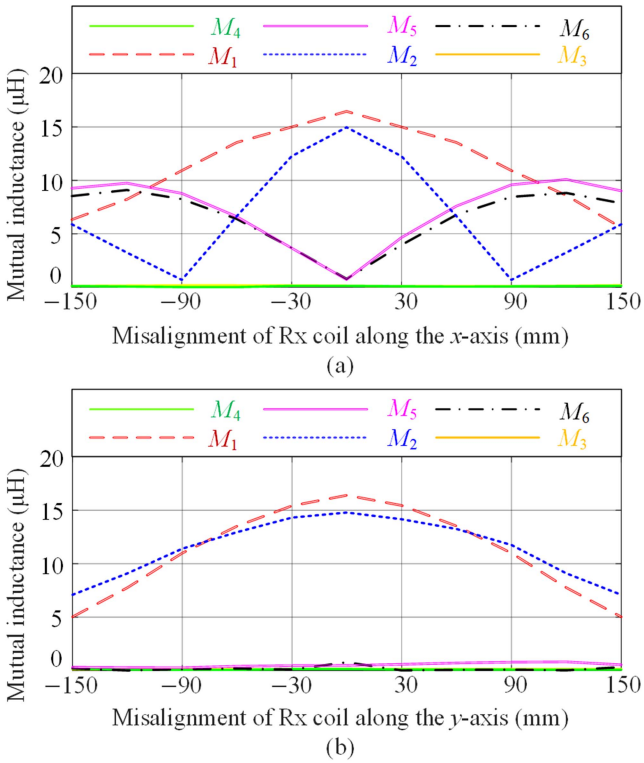

Fig. 4. Measurement of the mutual-inductance. (a) Misalignment along the *x*-axis. (b) Misalignment along the *y*-axis.

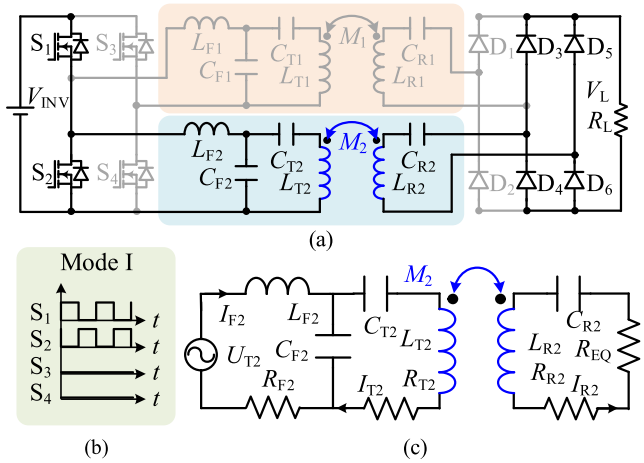

Fig. 5. WPT system in Mode I. (a) Circuit topology. (b) Switching timing. (c) Equivalent circuit.

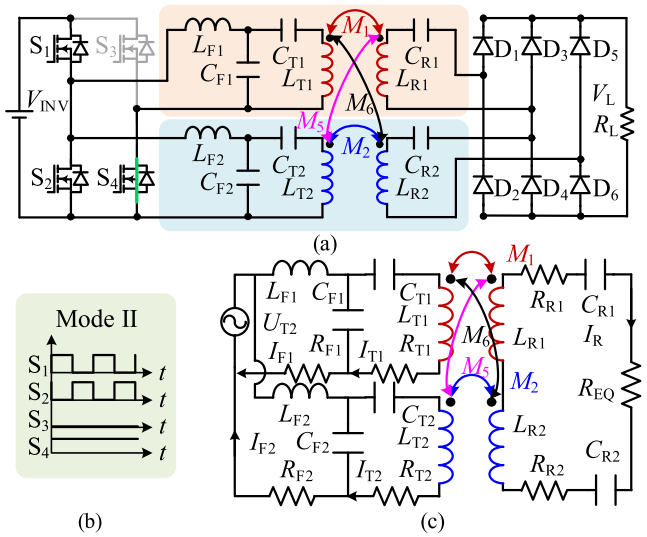

Fig. 6. WPT system in Mode II. (a) Circuit topology. (b) Switching timing. (c) Equivalent circuit.

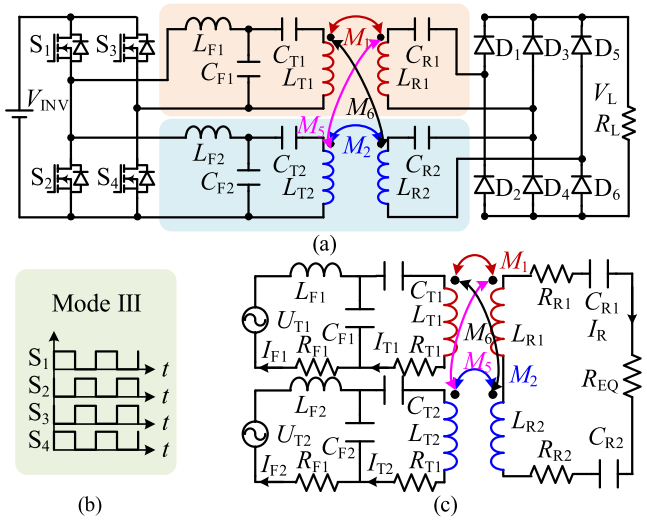

Fig. 7. WPT system in Mode III. (a) Circuit topology. (b) Switching timing. (c) Equivalent circuit.

[30]. This system should have high efficiency energy transmission, simple control strategies, no additional switching devices, rationality of the magnetic coupling structure, and high integration.

By summarizing the parameter data of the coupling structure on the Rx in the content of SAE J2954 [31], the dimensions and diameter of coil (Φ) of three different Rx coil structures under power class are summarized, as given in Table I. In the Z1 and Z3, the size of coupling structure and Φ vary greatly. Under the premise of meeting the standard coil parameters, three different coil structures need to be designed to meet the different power class scenarios. In the Z2, the differences in the dimensions and Φ of the three-power class coupling structures corresponding to WPT1, WPT2, and WPT3 are negligible. The premise of building an EV WPT system with power class interoperability is to ensure that the air gap of the coupling structure is Z2.

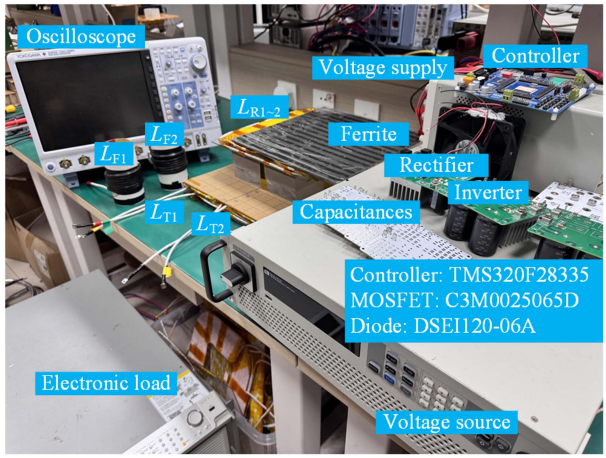

Fig. 8. Downscaled experimental prototype.

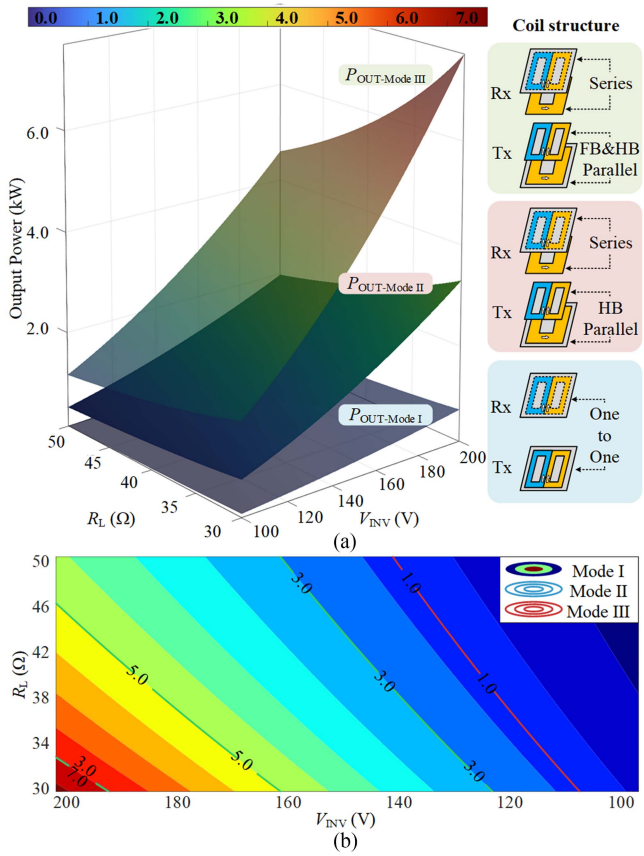

Fig. 9. Variation of output power with load and input voltage in three modes. (a) Three-dimensional visible view. (b) *XOY* surface mapping diagram.

The above application scenarios can be divided into: low-power battery protection (WPT1); cost-effective output of rated power (WPT2); and high-power emergency response (WPT3). This paper proposed a novel reconfigurable EV WPT system with power-class interoperability, as shown in Fig. 1, which has the following advantages.

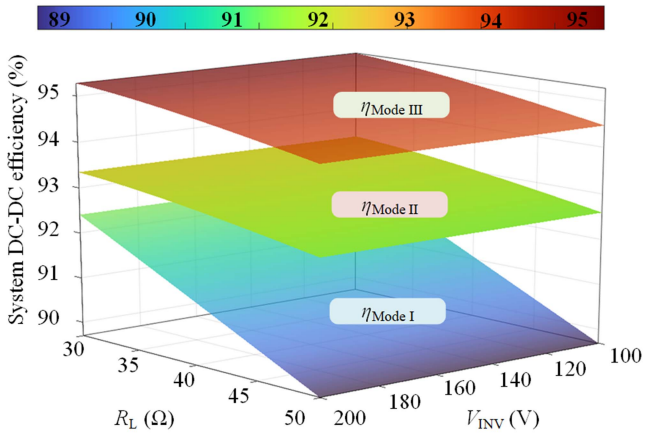

Fig. 10. Variation of system DC–DC efficiency with load and input voltage in three modes.

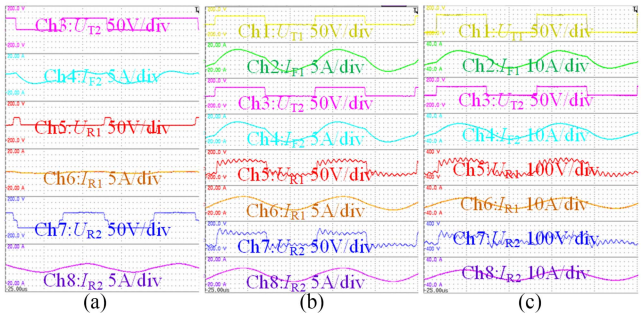

Fig. 11. Waveform diagram in the positive position. (a) Mode I. (b) Mode II. (c) Mode III.

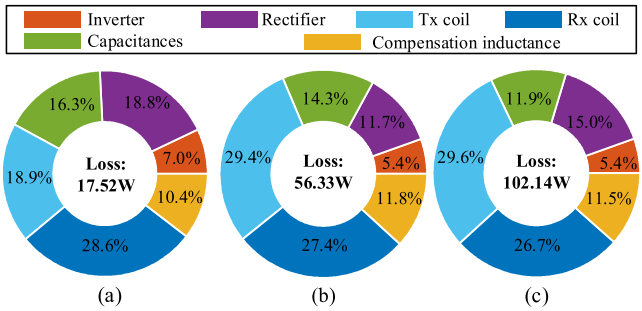

Fig. 12. System loss distribution diagram. (a) Mode I. (b) Mode II. (c) Mode III.

1) With the power-class interoperability.
2) The coupling structure is replaceable and has a relatively high level of scalability.
3) Simple control strategies, no additional switching devices.
4) High efficiency (>90%) energy transmission regardless of the working mode.

The rest of this paper is organized as follows. In Section II, the coupling structure has been presented. In Section III, the reconfigurable topology has been proposed, which is used to verify the power class interoperability. Section IV presents the experimental verification. Finally, Section V concludes the paper.

II. Magnetic Coupling Structure

The magnetic coupling structure adopted by the proposed WPT system is shown in Fig. 2. Tx and Rx also contain two kinds of coil structure, unipolar (Q) and bipolar (DD) coil, which is stacked on top of each other. The stacking forms of Q and DD coils are adopted.

Based on the number of coils at the Tx and Rx, the mutual inductance between the shown coils is defined as M_i ($i = 1, 2,\ldots,6$). By building a simulation model of the corresponding coupling structure in Maxwell, the magnetic field of the coupling structure is visualized. When placed in the positive position, it is shown in Fig. 3.

Using the coil parameters of the established simulation model, namely the size of the Tx and Rx coil (l) is 300 mm × 300 mm, airgap is 130 mm, the variation diagrams of all mutual inductances of the proposed coupling structure with the misalignment were measured and plotted, as shown in Fig. 4. When the Rx of the proposed coupling structure offsets along the x-axis or y-axis, M_3 and M_4 will not exhibit corresponding fluctuations, and the values will be almost zero, which can be disregarded.

III. Proposed Dual Channel Reconfigurable Topology

According to the definition of power class in SAE standard, mode I corresponds to WPT1 power class, Mode II corresponds to WPT2 power class, and mode III corresponds to WPT3 power class. The proposed reconfigurable topology further realizes the switching of three power classes by changing the conduction OFF state of S_1-S_4 without adding additional switching relays, so as to adapt to the interoperability of WPT1∼3. The self-inductance of the coupling structure can be defined in L_{T1}, L_{T2}, L_{R1}, and L_{R2}. L_{F1} and L_{F2} are the compensating inductances. C_{F1}, C_{F2}, C_{T1}, C_{T2}, C_{R1}, and C_{R2} are the compensating capacitances.

A. Mode I for WPT1

When the proposed system is working in Mode I for the WPT1 scenarios, the circuit topology is shown in Fig. 5(a). Based on the switching timing, as shown in Fig. 5(b), the equivalent circuit is shown in Fig. 5(c). V_{INV} (V_L) and U_{T2} are the inverter (rectifier) dc and fundamental ac voltages, respectively. R_{F2}, R_{T2}, and R_{R2} are the corresponding equivalent series resistances (ESRs) of L_{F2}, L_{T2}, and L_{R2}, respectively. R_{EQ} is the equivalent load resistance. They can be expressed as

$$U_{T2} = \frac{\sqrt{2}}{\pi} V_{\mathrm{INV}}, R_{\mathrm{EQ}} = \frac{8}{\pi^2} R_L. \tag{1}$$

The system works at the resonant angle frequency ω

$$\begin{aligned} \omega &= \frac{1}{\sqrt{L_{F1}C_{F1}}} = \frac{1}{\sqrt{L_{F2}C_{F2}}} = \frac{1}{\sqrt{L_{R1}C_{R1}}} \\ &= \frac{1}{\sqrt{L_{R2}C_{R2}}} = \sqrt{\frac{C_{F1}+C_{T1}}{L_{T1}C_{F1}C_{T1}}} = \sqrt{\frac{C_{F2}+C_{T2}}{L_{T2}C_{F2}C_{T2}}}. \end{aligned} \tag{2}$$

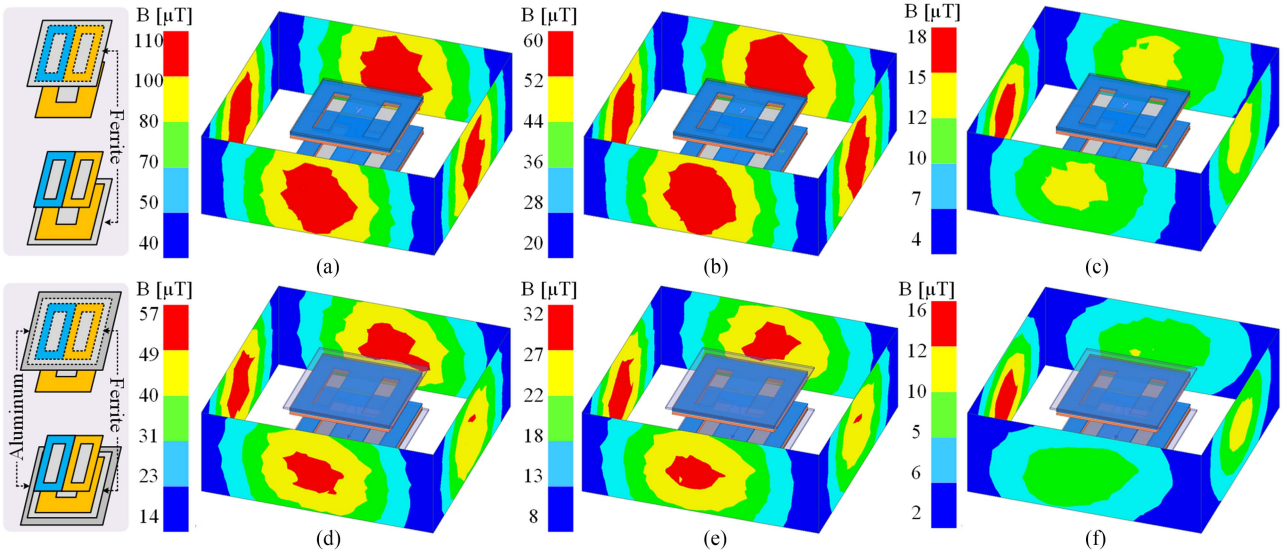

Fig. 13. Magnetic field distribution diagram during full-power operation simulation. (a) Mode I without aluminum plate. (b) Mode II without aluminum plate. (c) Mode III without aluminum plate. (d) Mode I with aluminum plate. (e) Mode II with aluminum plate. (f) Mode III with aluminum plate.

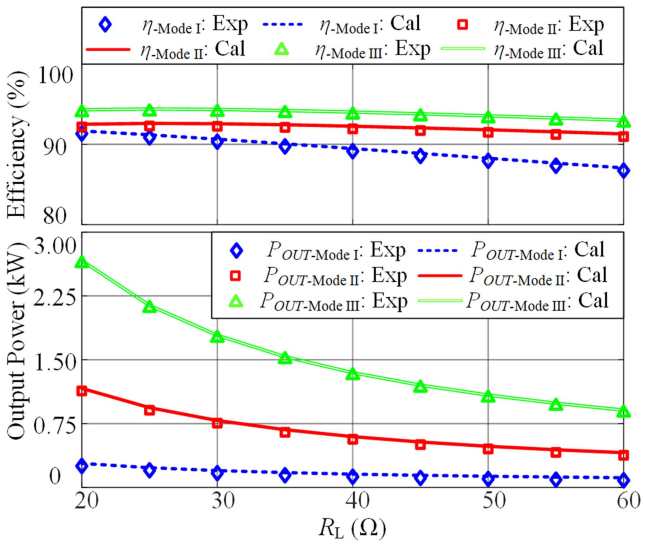

Fig. 14. System DC–DC efficiency and output power changes under different loads.

Using Kirchhoff's voltage law (KVL), can be expressed as

$$\begin{cases} U_{T2} = (j\omega L_{F2} + R_{F2})I_{F2} + \frac{1}{j\omega C_{F2}}(I_{F2} - I_{T2}) \\ \frac{1}{j\omega C_{F2}}(I_{F2} - I_{T2}) = (j\omega L_{T2} + \frac{1}{j\omega C_{T2}} + R_{T2})I_{T2} \\ -j\omega M_2 I_{R2} \\ j\omega M_2 I_{T2} = (j\omega L_{R2} + \frac{1}{j\omega C_{R2}} + R_{R2} + R_{\mathrm{EQ}})I_{R2} \end{cases}. \quad (3)$$

I_{F2}, I_{T2}, and I_{R2} are their corresponding currents, respectively. Ignoring ESRs, them can be expressed as

$$\begin{cases} I_{F2} = \frac{\omega^4 M_2^2 C_{F2}^2 U_{T2}}{R_{\mathrm{EQ}}} \\ I_{T2} = -j\omega C_{F2} U_{T2} \\ I_{R2} = \frac{\omega^2 M_2 C_{F2} U_{T2}}{R_{\mathrm{EQ}}} \end{cases}. \quad (4)$$

The system output power ($P_{\mathrm{OUT\text{-}Mode\ I}}$) can be expressed as

$$P_{\mathrm{OUT-Mode\ I}} = \frac{\omega^4 C_{F2}^2 {M_2}^2 U_{T2}^2}{4R_{\mathrm{EQ}}}. \quad (5)$$

The system dc–dc efficiency ($\eta_{\mathrm{Mode\ I}}$) can be expressed as

$$\eta_{\mathrm{Mode\ I}} = \frac{P_{\mathrm{OUT}}}{P_{\mathrm{OUT}} + I_{F2}^2 R_{F2} + I_{T2}^2 R_{T2} + I_{R2}^2 R_{R2}}. \quad (6)$$

B. Mode II for WPT2

When the proposed WPT system is working in Mode II for the WPT2 scenarios, the proposed system and equivalent circuit are shown in Fig. 6. In this mode, when the system undergoes offset, the cross-coupling cannot be ignored. To fit the actual application scenarios, the cross-coupling M_5 and M_6 between the two channels are introduced. Through KVL, and ignoring ESRs, corresponding currents can be expressed as

$$\begin{cases} I_{F1} = \frac{\omega^4[(M_1+M_6)^2 C_{F1}^2 + (M_1+M_6)(M_2+M_5)C_{F1}C_{F2}]U_{T2}}{R_{\mathrm{EQ}}} \\ I_{T1} = -j\omega C_{F1} U_{T2} \\ I_{F2} = \frac{\omega^2[(M_1+M_6)(M_2+M_5)C_{F1}C_{F2} + (M_2+M_5)^2 C_{F2}^2]U_{T2}}{R_{\mathrm{EQ}}} \\ I_{T2} = -j\omega C_{F2} U_{T2} \\ I_R = \frac{\omega^2[(M_1+M_6)C_{\mathrm{F1}} + (M_2+M_5)C_{F2}]U_{T2}}{R_{\mathrm{EQ}}} \end{cases}. \quad (7)$$

The $P_{\mathrm{OUT\text{-}Mode\ II}}$ can be expressed as

$$P_{\mathrm{OUT-Mode\ II}} = \frac{\omega^4[(M_1+M_6)C_{F1} + (M_2+M_5)C_{F2}]^2 U_{T2}^2}{R_{\mathrm{EQ}}}. \quad (8)$$

The $\eta_{\mathrm{Mode\ II}}$ can be expressed as

$$\eta_{\mathrm{Mode\ II}} = \frac{P_{\mathrm{OUT}}}{P_{\mathrm{OUT}} + \sum_{i=1}^{2}(I_{Fi}^2 R_{Fi} + I_{Ti}^2 R_{Ti}) + I_R^2(R_{R1} + R_{R2})}. \quad (9)$$

C. Mode III for WPT3

When the WPT system is working in mode III for the WPT3 scenarios, the proposed system and equivalent circuit are shown in Fig. 7. U_{T1} is the fundamental ac voltage, which can be expressed as

$$U_{\mathrm{T1}} = \frac{2\sqrt{2}}{\pi} V_{\mathrm{INV}} = 2U_{T2}. \tag{10}$$

Through KVL, and ignoring ESRs, while retaining the cross-coupling between the two channels, corresponding currents can be expressed as

$$\begin{cases} I_{F1} = \frac{\omega^4[2(M_1+M_6)^2 C_{F1}^2 + (M_1+M_6)(M_2+M_5)C_{F1}C_{F2}]U_{T2}}{R_{\mathrm{EQ}}} \\ I_{T1} = -2j\omega C_{F1} U_{T2} \\ I_{F2} = \frac{\omega^2[2(M_1+M_6)(M_2+M_5)C_{F1}C_{F2} + (M_2+M_5)^2 C_{F2}^2]U_{T2}}{R_{\mathrm{EQ}}} \\ I_{T2} = -j\omega C_{F2} U_{T2} \\ I_R = \frac{\omega^2[2(M_1+M_6)C_{F1} + (M_2+M_5)C_{F2}]U_{T2}}{R_{\mathrm{EQ}}} \end{cases}. \tag{11}$$

The $P_{\mathrm{OUT\text{-}\ Mode\ III}}$ can be expressed as

$$P_{\mathrm{OUT–Mode\ III}} = \frac{\omega^4[2(M_1+M_6)C_{F1} + (M_2+M_5)C_{F2}]^2 U_{T2}^2}{R_{\mathrm{EQ}}}. \tag{12}$$

The $\eta_{\mathrm{Mode\ III}}$ can be expressed as

$$\eta_{\mathrm{Mode\ III}} = \frac{P_{\mathrm{OUT}}}{P_{\mathrm{OUT}} + \sum_{i=1}^{2}(I_{Fi}^2 R_{Fi} + I_{Ti}^2 R_{Ti}) + I_R^2(R_{R1}+R_{R2})}. \tag{13}$$

Three modes can meet three different power class scenarios of WPT1∼3 under the premise of keeping the input voltage and load resistance constant. At the same time, the proposed EV WPT system has high robustness for adding additional relay switches and resetting complex resonant relationships.

IV. Experimental Validation

A. Experimental Platform

A 1.6-kW downscaled WPT system was constructed to validate the proposed method, as shown in Fig. 8. Meanwhile, the key components adopted by the system have also been marked. This section introduces multiple sets of experiments based on the experimental system, respectively elaborating on the verification of the downscaled prototype, power class interoperability, electromagnetic radiation analysis, load variability, and misalignment tolerance characteristics. The corresponding parameters of the final presented system are shown in Table II. In combination with the standard parameters of the coupling structure for different power classes in Table I, a coil with the Φ of 5.0 mm is adopted here as the corresponding coupling structure for the downscaled experimental prototype.

B. Downscaling Verification

Based on the P_{OUT} and η in the Section III, the variation of output power and system dc–dc efficiency changes with load and input voltage are obtained, as shown in Figs. 9 and 10. Based on the parameters of the downscaled experimental prototype, when the input voltage is 200 V and the load is 30 Ω, the calculated output power of modes I, II, and III is 0.75 kW, 3.30 kW, and 7.67 kW, respectively, the calculated system dc–dc efficiency of modes I, II, and III is 92.41%, 93.34%, and 95.27%, respectively. The above three modes can meet three different power-class scenarios of WPT1∼3. The proposed WPT system has high robustness for adding additional relay switches and resetting complex resonant relationships.

TABLE II
Parameters of Experimental Prototype

Symbol	Parameter	Value
L_{F1}	Filtering inductor on channel 1	10.0 μH
C_{F1}	Filtering capacitor on channel 1	351.70 nF
R_{F1}	Parasitic resistance of L_{F1}	37.10 mΩ
L_{T1}	Resonant inductor on channel 1	66.52 μH
C_{T1}	Resonant capacitor on channel 1	62.14 nF
R_{T1}	Parasitic resistance of L_{T1}	118.40 mΩ
L_{F2}	Filtering inductor on channel 2	10.0 μH
C_{F2}	Filtering capacitor on channel 2	350.30 nF
R_{F2}	Parasitic resistance of L_{F2}	37.20 mΩ
L_{T2}	Resonant inductor on channel 2	76.16 μH
C_{T2}	Resonant capacitor on channel 2	52.98 nF
R_{T2}	Parasitic resistance of L_{T2}	135.60 mΩ
L_{R1}	Resonant inductor on the RxQ	57.75 μH
C_{R1}	Resonant capacitor on the RxQ	60.77 nF
R_{R1}	Parasitic resistance of L_{R1}	102.80 mΩ
L_{R2}	Resonant inductor on the RxDD	89.31 μH
C_{R2}	Resonant capacitor on the RxDD	39.29 nF
R_{R2}	Parasitic resistance of L_{R2}	159.00 mΩ

TABLE III
Experimental Results

Mode		I	II	III
V_{INV}		100 V		
R_{L}		30 Ω		
f		85 kHz		
P_{OUT}		163.47W	669.63W	1605.88W
η_{max}		90.32%	92.24%	94.02%
ZVS		√	√	√
Coupling Structure	Tx	DD coil	Q and DD coil	Q and DD coil
	Rx	DD coil	Q and DD coil	Q and DD coil
Scenario		WPT1	WPT2	WPT3

TABLE IV
Reference Levels for Occupational Exposure to Time-Varying Electric and Magnetic Fields (Unperturbed RMS Values)

Frequency	E-field E (kV/m)	Magnetic field H (A/m)	Magnetic flux B (T)
1-8 Hz	20	$1.63\times10^5/f^2$ *	$0.2/f^2$
8-25 Hz	20	$2.0\times10^4/f$	$2.5\times10^{-2}/f$
25-300 Hz	$5.0\times10^2/f$	8.0×10^2	1.0×10^{-3}
0.3-3 kHz	$5.0\times10^2/f$	$2.4\times10^5/f$	$0.3/f$
0.003-10 MHz	1.7×10^{-1}	80	1.0×10^{-4}

Notes: *f in Hz.

C. Power Class Interoperability

Based on the downscaled experimental prototype, the experimental results are shown in Table III. When the input voltage is 100 V and the load is 30 Ω. When the system works in Mode I and is in the positive position, the system output power is 163.47 W and the dc–dc efficiency is 90.31%. Meanwhile, the current and voltage waveform of each branch of the system is shown in Fig. 11(a), and the system realizes ZVS.

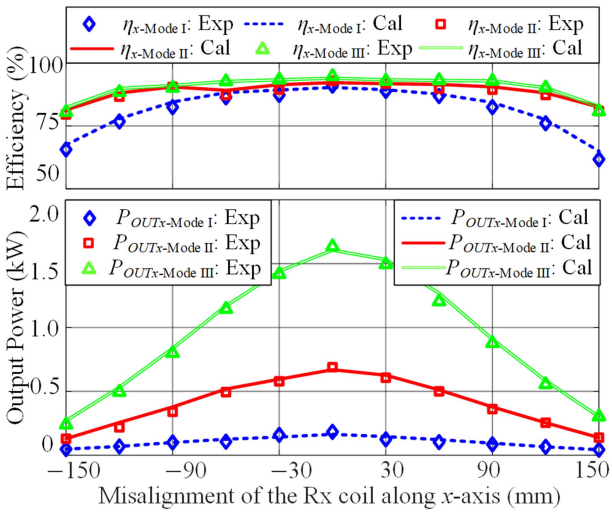

Fig. 15. System DC–DC efficiency and output power changes offset along the *x*-axis.

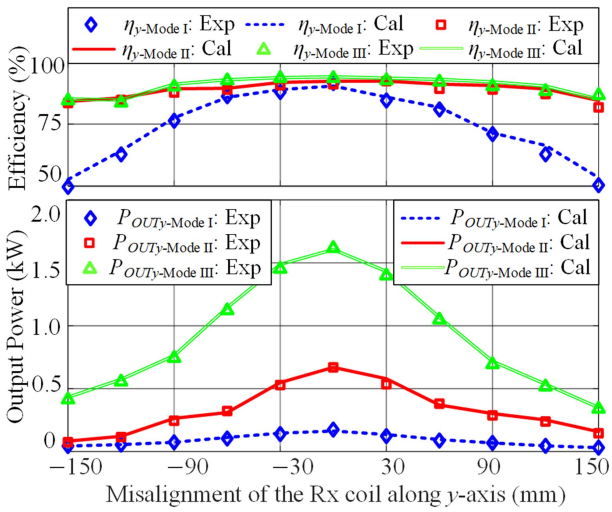

Fig. 16. System DC–DC efficiency and output power changes offset along the *y*-axis.

When the system works in Mode II and is in the positive position, the output power is 669.62 W, and the system dc–dc efficiency is 92.23%. Meanwhile, the current and voltage waveform of each branch of the system is shown in Fig. 11(b), and the system realizes ZVS.

When the system works in Mode III and is in the positive position, the system output power is 1605.88 W, and the system dc–dc efficiency is 94.02%. At this time, the current and voltage waveform of each branch of the system is shown in Fig. 11(c), and the system realizes ZVS.

The power loss distributions under different working conditions are shown in Fig. 12. The power lost by the system under different working conditions is mainly concentrated inside the Tx and Rx coils, that is, the internal circulating current is relatively high. In the case of mode I, proposed system is affected by cross-coupling. Not only will it generate corresponding circulating losses at the Tx of channel one, but it will also cause unnecessary losses on the Rx, thereby reducing the transmission efficiency of the entire system. The proposed system can not only achieve high efficiency output of three modes under the premise of ZVS, but also meet the system output power of WPT1∼3 application scenarios.

D. Electromagnetic Radiation Analysis

Based on the output mode of the mentioned EV WPT system itself, the electromagnetic radiation of the system is analyzed here. First, in combination with the ICNIRP standard, the reference levels (unperturbed RMS values) of public exposure to time-varying electric and magnetic fields as given in Table IV were obtained [32]. By integrating the power-class interoperability performance of the proposed system, the magnetic field distribution was simulated respectively under the conditions of adding additional shielding (aluminum plate) and for adding additional shielding.

Based on the WPT system parameters proposed in Table II, the visual magnetic field distribution diagrams of each working mode at full power operation were simulated respectively (compared with the power of the downscaled prototype), as shown in Fig. 13.

By taking the magnetic field conditions at 20 cm from the edge of the coupling structure, respectively [32], it can be concluded that the system meets the maximum magnetic field strength requirements in the standard without adding aluminum plate shielding. At the same time, after adding additional aluminum plates, the overall magnetic field strength of the system was weakened.

E. Load Variability

To describe the transmission characteristics of the proposed system, it can be known from (4), (7), and (11) that the proposed system has the transmission characteristic of constant voltage output. By changing the variations of the system load with the 100 V input voltage, the changes in the system dc–dc efficiency and output power are shown in Fig. 14. With the linear variation of the load resistance, the system output characteristics in the three modes of the proposed system show a decreasing trend with the increase of the load.

F. Misalignment Tolerance

The system dc–dc efficiency and output power changes presented when the system is offset along the *x*-axis and *y*-axis under the working state of the proposed system in modes I, II, and III respectively are shown in Figs. 15 and 16, respectively. Correspondingly, the system waveform diagrams of the coupling structures at 30, 60, and 90 mm, respectively, in each mode are shown in Fig. 17, all of which have achieved ZVS. When the system is offset along the *x*-axis, no matter which mode the system works in, it can achieve system dc–dc efficiency of more than 75% in the range of ±120 mm [31].

When the system is offset along the *y*-axis, the system works in Mode I and Mode II, and can achieve dc–dc efficiency of more than 75% in the range of ±150 mm. When the system works in

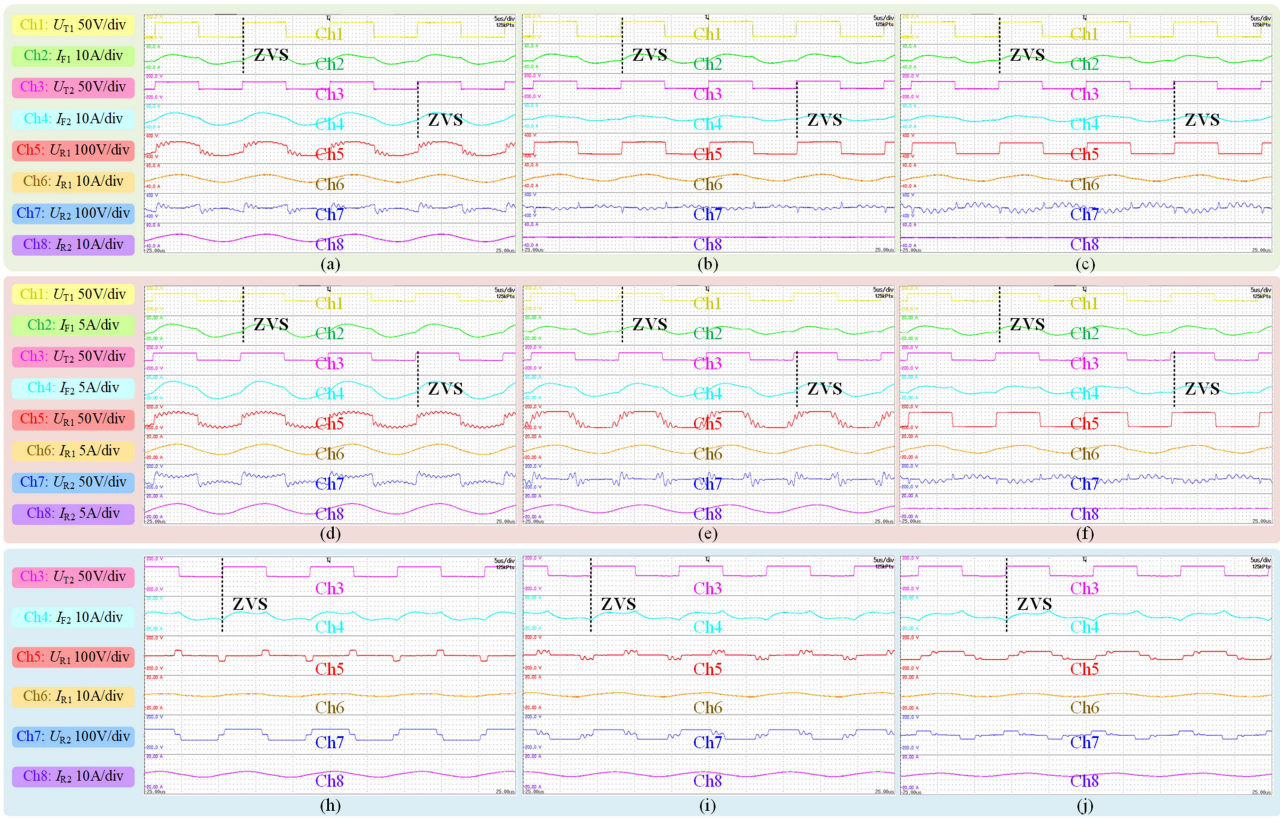

Fig. 17. Waveform diagram in 30, 60, and 90 mm. (a)–(c) Mode I. (d)–(f) Mode II. (h)–(j) Mode III.

TABLE V
COMPARISON AMONG DIFFERENT TOPOLOGIES

Refs		[29]	[30]	This Work
Topology		LLC-Dual LLC	Dual LCC-LCC	Dual LCC-S
Rated power		50.0 kW	30.0 kW	1.6 kW
Power class interoperability		√	√	√
The number of	Working Mode	2	3	3
	Inverter	12	8	4
	Additional switches	0	4	0
Magnetic coupling structure	Tx	585×560 mm	1064×910 mm	300×300 mm
	Rx	585×560 mm	590×448 mm 576×460 mm 800×610 mm	300×300 mm
	Φ	10.0 mm	NA	5.0 mm
	Airgap	160 mm	71, 101, 185 mm	130 mm
Misalignment tolerance (η> 75%)*		±75 mm (x-axis) ±100 mm (y-axis)	NA	±120 mm (x-axis) ±90 mm (y-axis)
Maximum system DC-DC efficiency		92.00% (10.0 kW) 94.00% (50.0 kW)	94.00% (6.0 kW) 94.70% (11.0 kW) 93.60% (30.0 kW)	90.32% (Mode I) 92.24% (Mode II) 94.02% (Mode III)

Note: *According to the SAE J2954 standard, the efficiency of WPT1 (3.3 kW) should reach more than 75% in the case of maximum deviation, and WPT2 (7.7 kW) should reach more than 77% [31].

Mode III, it can achieve more than 75% system dc–dc efficiency transmission in the range of ±90 mm.

Based on the different enabling states of the coupling structure corresponding to different modes of the proposed system, it is confirmed here that the coupling structure of the Q and DD coil stacking method adopted has a certain degree of misalignment tolerance characteristics. At the same time, the proposed system itself has a relatively high level of scalability, which only used Q and DD coils as the magnetic coupling structure. Subsequently, by replacing the complex coil structure, the system can possess a higher level of misalignment tolerance characteristics and stable output capacity.

G. Comparisons

The results of the comparisons with existing works are shown in Table V. The proposed WPT system, while having the performance of power-class interoperability, has a very small number of inverters and still ensures more power-class scenarios. The proposed system adopts a magnetic coupling structure that only

needs to meet the requirement of mutual decoupling, which has a high degree of design freedom and reduces the design difficulty at the level of coupling structure design.

This paper confirms the power-class interoperability performance of the proposed WPT system with its output voltage and magnetic coupling structure. In the future, by completely eliminating cross-coupling through changes to the coil structure and integrating it with the proposed wireless power transmission system, it will be possible to further improve the defects existing in the coupling structure while achieving the effects described in this paper.

V. Conclusion

This paper has proposed a novel reconfigurable topology with power class interoperability. Three modes can be switched by the inverter timing without adding other relay switches. A 1.6-kW downscaled experimental prototype have been built. The power-class interoperability performance with WPT1∼3 scenarios was verified. The experimental results have demonstrated the superiority of the proposed system in power class interoperability. When the system input voltage is 100 V, the dc–dc efficiency corresponding to the three modes of the system is 90.31%, 92.23%, and 94.02%, respectively. Regardless of which mode the proposed system operates in, it remains within the safe range of electromagnetic radiation. With the offset occurred, the system can maintain high efficiency whenever in any operating modes.

References

[1] H. Wang et al., "Blind-zone-free metal object detection system for wireless EV charging system employing strip multipolar detection coils," *IEEE Trans. Transport. Electrif.*, vol. 11, no. 1, pp. 4420–4428, Feb. 2025, doi: 10.1109/TTE.2024.3462439.

[2] P. Vishnuram, P. S., R. N., K. V., and B. Nastasi, "Wireless Chargers for electric vehicle: A systematic review on converter topologies, environmental assessment, and review policy," *Energies*, vol. 16, no. 4, 2023, Art. no. 1731, doi: 10.3390/en16041731.

[3] Z. Yan et al., "An underwater wireless power transfer system with improved misalignment tolerance," *IEEE J. Emerg. Sel. Topics Power Electron.*, vol. 13, no. 4, pp. 4369–4376, Aug. 2025, doi: 10.1109/JESTPE.2025.3541289.

[4] H. Tang et al., "A self-adaptive dual-channel LCC-S detuned topology for misalignment tolerance in AUV wireless power transfer systems," *IEEE Trans. Power Electron.*, vol. 40, no. 3, pp. 4630–4639, Mar. 2025, doi:10.1109/TPEL.2024.3492194.

[5] A. Zakerian, S. Vaez-Zadeh, and A. Babaki, "A dynamic WPT system with high efficiency and high power factor for electric vehicles," *IEEE Trans. Power Electron.*, vol. 35, no. 7, pp. 6732–6740, Jul. 2020, doi: 10.1109/TPEL.2019.2957294.

[6] W. Chen, J. Jia, X. Yan, Y. Song, and J. Li, "Wireless power supply based on MNG-MNZ metamaterial for cardiac pacemakers," *CES Trans. Elect. Machines Syst.*, vol. 8, no. 1, pp. 103–112, Mar. 2024.

[7] C. Liu, M. Zhou, R. Xie, X. Chen, X. Mao, and Y. Zhang, "An interoperable receiver with reconfigurable LCC compensation for wireless charging of 400- and 800-V batteries in electric vehicles," *IEEE Trans. Ind. Electron.*, vol. 72, no. 8, pp. 8710–8714, Aug. 2025, doi: 10.1109/TIE.2025.3528476.

[8] B. Zhang, J. Deng, and Z. Wang, "An interoperable and high-efficiency wireless electric vehicle charger based on reconfigurable topology," *IEEE Trans. Power Electron.*, vol. 39, no. 10, pp. 14039–14053, Oct. 2024, doi: 10.1109/TPEL.2024.3425603.

[9] Y. Wu et al., "An integrated charger of wireless power transfer, onboard charger, and auxiliary power module for electric vehicles," *IEEE Trans. Power Electron.*, vol. 40, no. 4, pp. 6334–6344, Apr. 2025, doi: 10.1109/TPEL.2024.3518499.

[10] Electric Power Research Institute. Accessed: Oct. 24, 2025. [Online]. Available: https://www.epri.com/research/products/000000003002028811

[11] A. Zahedmanesh, K. M. Muttaqi, and D. Sutanto, "Coordinated charging control of electric vehicles while improving power quality in power grids using a hierarchical decision-making approach," *IEEE Trans. Veh. Technol.*, vol. 69, no. 11, pp. 12585–12596, Nov. 2020, doi: 10.1109/TVT.2020.3025809.

[12] J. A. A. Silva, J. Camilo López, N. Bañol Arias, L. Zenichi Terada, and M. J. Rider, "Tri-level adaptive robust optimization for the optimal charging coordination of EVs considering grid impact," *IEEE Access*, vol. 12, pp. 169755–169767, 2024, doi: 10.1109/ACCESS.2024.3498600.

[13] M. M. Ahmed, M. A. Enany, A. A. Shaier, H. M. Bawayan, and S. A. Hussien, "An extensive overview of inductive charging technologies for stationary and In-motion electric vehicles," *IEEE Access*, vol. 12, pp. 69875–69894, 2024, doi: 10.1109/ACCESS.2024.3402553.

[14] Z. Shen, R. Xie, C. Liu, X. Yu, X. Cheng, and Y. Zhang, "An electric vehicle wireless charging system with 400-V and 800-V battery tolerance and strong offset resistance," *IEEE Trans. Power Electron.*, vol. 40, no. 4, pp. 4722–4726, Apr. 2025, doi: 10.1109/TPEL.2024.3516715.

[15] X. Yu et al., "Compact wireless power transfer with enhanced misalignment tolerance via independent secondary PWM control," *IEEE Trans. Power Electron.*, vol. 40, no. 9, pp. 11998–12002, May 2025, doi: 10.1109/TPEL.2025.3570846.

[16] R. Xie et al., "A simple integrated solution of reconfigurable wired and wireless vehicle-to-vehicle (V2V) charging system," *Wireless Power Transfer*, vol. 11, no. 1, Nov. 2024, Art. no. e011.

[17] Y. Hu, C. Chen, T. He, J. He, X. Guan, and B. Yang, "Proactive power management scheme for hybrid electric storage system in EVs: An MPC method," *IEEE Trans. Intell. Transp. Syst.*, vol. 21, no. 12, pp. 5246–5257, Dec. 2020, doi: 10.1109/TITS.2019.2952678.

[18] P. Kaloriya, N. Gupta, S. Vashisth, K. R. Niazi, and A. Swarnkar, "A new strategy for potential smart grids to alleviate heavy EV charging demand in residential areas," in *Proc. 14th Int. Conf. Comput. Commun. Netw. Technol.*, 2023, pp. 1–6, doi: 10.1109/ICCCNT56998.2023.10307293.

[19] H. Feng, R. Tavakoli, O. C. Onar, and Z. Pantic, "Advances in high-power wireless charging systems: Overview and design considerations," *IEEE Trans. Transp. Electrif.*, vol. 6, no. 3, pp. 886–919, Sep. 2020, doi: 10.1109/TTE.2020.3012543.

[20] H. Wouters and W. Martinez, "Bidirectional onboard chargers for electric vehicles: State-of-the-art and future trends," *IEEE Trans. Power Electron.*, vol. 39, no. 1, pp. 693–716, 2024, doi: 10.1109/TPEL.2023.3319996.

[21] S. Kim, G. A. Covic, and J. T. Boys, "Comparison of tripolar and circular pads for IPT charging systems," *IEEE Trans. Power Electron.*, vol. 33, no. 7, pp. 6093–6103, Jul. 2018, doi: 10.1109/TPEL.2017.2740944.

[22] A. U. Ibrahim, W. Zhong, and M. D. Xu, "A 50-kW three-channel wireless power transfer system with low stray magnetic field," *IEEE Trans. Power Electron.*, vol. 36, no. 9, pp. 9941–9954, Sep. 2021, doi: 10.1109/TPEL.2021.3064373.

[23] J. Pries, V. P. N. Galigekere, O. C. Onar, and G. Su, "A 50-kW three-phase wireless power transfer system using bipolar windings and series resonant networks for rotating magnetic fields," *IEEE Trans. Power Electron.*, vol. 35, no. 5, pp. 4500–4517, May 2020, doi: 10.1109/TPEL.2019.2942065.

[24] W. Zhong, S. Zhang, M. Chen, and M. D. Xu, "Reconfigurable resonant topology linking two-, three-, and four-coil modes for WPT with large coupling range and fixed frequency," *IEEE Trans. Power Electron.*, vol. 37, no. 7, pp. 8713–8725, Jul. 2022, doi: 10.1109/TPEL.2022.3148001.

[25] H. H. Wu, A. Gilchrist, K. D. Sealy, and D. Bronson, "A high efficiency 5 kW inductive charger for EVs using dual side control," *IEEE Trans. Ind. Inform.*, vol. 8, no. 3, pp. 585–595, Aug. 2012, doi: 10.1109/TII.2012.2192283.

[26] X. Zhang et al., "A control strategy for efficiency optimization and wide ZVS operation range in bidirectional inductive power transfer system," *IEEE Trans. Ind. Electron.*, vol. 66, no. 8, pp. 5958–5969, Aug. 2019, doi: 10.1109/TIE.2018.2871794.

[27] M. Wu et al., "A dual-sided control strategy based on mode switching for efficiency optimization in wireless power transfer system," *IEEE Trans. Power Electron.*, vol. 36, no. 8, pp. 8835–8848, Aug. 2021, doi: 10.1109/TPEL.2021.3055963.

[28] M. Mohammad et al., "Bidirectional *LCC –LCC* -compensated 20-kW wireless power transfer system for medium-duty vehicle charging," *IEEE Trans. Transp. Electrif.*, vol. 7, no. 3, pp. 1205–1218, Sep. 2021, doi: 10.1109/TTE.2021.3049138.

[29] P. A. J. Lawton, F. J. Lin, and G. A. Covic, "A power class interoperable multi-coil inductive power transfer system for 10/50 kW EV charging," *IEEE Open J. Power Electron.*, vol. 6, pp. 10–27, 2025, doi: 10.1109/OJPEL.2024.3514519.

[30] B. Zhang et al., "Design and implementation of interoperable high-efficiency bidirectional wireless power transfer systems for multiple vehicles," *Green Energy Intell. Transp.*, 2025, Art. no. 100307, doi: 10.1016/j.geits.2025.100307.

[31] Wireless Power Transfer for Light-Duty Plug-in/Electric Vehicles and Alignment Methodology, SAE J2954 standard. Accessed: Dec. 12, 2024. [Online]. Available: www.sae.org/standards/content/j2954_202010/

[32] Statement on RF Knowledge Gaps-2025, ICNIRP Statement. Accessed: Jul. 12, 2025. [Online]. Available: www.icnirp.org/en/publications/index.html

Chao Liu was born in Shanxi, China, in 1997. He is currently working toward the Ph.D. degree in power electronics with the School of Electrical Engineering and Automation, Fuzhou University, Fuzhou¸ China.

His research interests include power electronics converters and wireless power transfer.

Mingzhu Zhou was born in Hubei, China. She received the B.S. degree in building electrical and intelligent and M.S. degree in control science and control engineering from Qingdao University of Technology, Qingdao, China, in 2018 and 2022, respectively. She is currently working toward the Ph.D. degree in power electronics with the School of Electrical Engineering and Automation, Fuzhou University, Fuzhou¸ China.

Her research interests include power electronic power conversion technology and soft-switching techniques.

Yizhan Zhuang (Member, IEEE) was born in Fujian, China, in 1994. He received the B.S. degree in electrical engineering from the College of Electrical Engineering and Automation, Fuzhou University, Fuzhou, China, in 2017, and the Ph.D. degree in electrical engineering from the School of Electrical Engineering, Wuhan University, Wuhan, China, in 2023.

He is currently a Lecturer (Associate Researcher) with the School of Electrical Engineering and Automation, Fuzhou University, Fuzhou, China. His research interests include dc–dc power converter and interface of photovoltaic conversion systems.

Xiangpeng Cheng (Member, IEEE) received the B.S. and Ph.D. degrees in electrical engineering and automation from Xi'an Jiaotong University, Xi'an, China, in 2016 and 2022, respectively.

He was a Faculty Member in electrical engineering with Fuzhou University, where he is currently a Lecturer. From 2022 to 2024, he was with Economic and Technical Research Institute, State Grid Fujian Electric Power Company Ltd., as a Researcher. His research interests include high-frequency modeling, intelligent control, and stability analyses methods for power converters and electronified power systems, and micro-grids for sustainable energy and distributed generation.

Xingkui Mao (Member, IEEE) received the B.E. and Ph.D. degrees in electrical engineering from Fuzhou University, Fuzhou, China, in 2000 and 2006, respectively.

He is currently a Professor with the College of Electrical Engineering and Automation, Fuzhou University. His research interests include design, manufacturing, and control for power electronic system and components.

Dr. Mao was the recipient of one IEEE prize paper.

Yiming Zhang (Senior Member, IEEE) received the B.S. and Ph.D. degrees in electrical engineering from Tsinghua University, Beijing, China, in 2011 and 2016, respectively.

Afterward, he was a Postdoctoral Researcher with San Diego State University, San Diego, CA, USA and a Research Fellow with Nanyang Technological University, Singapore. He is currently a Full Professor with Fuzhou University. He has authored 1 book from Springer, authored or co-authored more than 100 technical papers in journals and conference proceedings. His research interests include wireless power transfer and resonant converters.

Dr. Zhang was the recipient of the Outstanding Doctoral Dissertations of Tsinghua University in 2016. He was recognized as an Outstanding Reviewer for IEEE TRANSACTIONS ON POWER ELECTRONICS in 2019 and 2022, and a Distinguished Reviewer for IEEE TRANSACTIONS ON INDUSTRIAL ELECTRONICS in 2020. He was the Publication Chair of the international conference ICWPT2022.